UNIVERSITY OF LEEDS

White Rose
university consortium
Universities of Leeds, Sheffield & York

eprints@whiterose.ac.uk
https://eprints.whiterose.ac.uk/

Effect of Al_2O_3 nanoparticle dispersion on the specific heat capacity of a eutectic binary nitrate salt for solar power applications

Yanwei Hu[1], Yurong He[1]*, Zhenduo Zhang[1], Dongsheng Wen[2, 3]

1, School of Energy Science & Engineering, Harbin Institute of Technology, Harbin, China, 150001

2, School of Aeronautic Science and Engineering, Beihang University, Beijing, China, 100191

3, School of Chemical and Process Engineering, University of Leeds, Leeds, U.K., LS2 9JT

*Corresponding author: Yurong He

Email: rong@hit.edu.cn

Tel. +86 0451 86413233; Fax +86 0451 86413233

Abstract: Molten salts can be used as heat transfer fluids or thermal storage materials in a concentrated solar power plant. Improving the thermal properties can influence the utilization efficiency of solar energy. In this study, the effect of doping eutectic binary salt solvent with Al_2O_3 nanoparticles on its specific heat capacity (c_p) was investigated. The effects of the mass fraction of nanoparticles on the c_p of the composite nanofluid were analyzed, using both differential scanning calorimetry measurements and molecular dynamics simulations. The specific heat capacity of the nanocomposites was enhanced by increasing the nanoparticle concentration. The maximum enhancement was found to be 8.3%, at a nanoparticle concentration of 2.0%. A scanning electron microscope was used to analyze the material morphology. It was observed that special nanostructures were formed and the specific heat capacity of the nanocomposites was enhanced by increasing the quantity of nanostructures. Simulation results of c_p agreed well with the experimental data, and the potential energy and interaction energy in the system were analyzed. The change in Coulombic energy contributed to most of the large change in c_p, which explains the discrepancy in values between conventional nanofluids and molten salt-based nanofluids.

Keywords: solar energy application; nanocomposite; specific heat capacity; molecular dynamics simulation; potential energy analysis

1. Introduction

The depletion of fossil fuels and the harmful gas emissions during the burning of fossil fuels compel the search for renewable and clean energy sources and higher efficiency of energy utilization [1–3]. To solve the energy crisis, some researchers focus on improving heat transfer efficiency via optimizing the heat transfer surface [4–7] while others tend to using high performance working media [8,9]. Meanwhile, the development of renewable energy was investigated. Solar energy is regarded as the best potential source to replace fossil fuels, with the average amount of energy transported to the earth as sunlight in one hour able to provide all of the energy currently consumed globally in one year [10]. A promising technology for the collection and use of solar energy is the concentrating solar power (CSP) system, which transforms solar energy to thermal energy with a heat-transfer fluid (HTF) [11]. Mahian et al.[12,13] used different working fluids in solar collectors and investigated the thermal efficiency. In solar collectors, lower specific heat capacity will induce a higher outlet temperature, increasing the solar energy utilization efficiency. However, solar energy is quite unsteady and unpredictable, since it varies from day to night, by cloud condition, and season. Hence, a working medium is needed to store the energy when it is available and then release it when there is insufficient sunlight. Considering the large amount of HTF and thermal energy storage (TES) materials required in a CSP plant, it is necessary to reduce the cost of these materials while improving their heat transfer and thermal storage performance. With thermal stability, comparable viscosity, and low vapor pressure at high temperature, various molten salts are used in modern CSP systems [14]. Solar salt, with a composition of 60% $NaNO_3$ and 40% KNO_3 by weight, was used in the Solar Two central receiver systems [15] and other solar plants [16]. Other molten salts are also being researched to improving the thermal performance [17–19].

However, these molten salts also have some disadvantages that limit the applicability of solar plants, for instance relatively low specific heat capacity and thermal conductivity [20]. Doping base fluids with nanosized particles to make nanofluids [21] is a potential way to improve their thermal properties, especially thermal conductivity [22]. Wen et al. [23] reviewed the heat transfer applications of nanofluids, including their formulations, influences on the effective thermal conductivity, and enhancement mechanisms. In previous research, various mechanisms have been identified that could enhance the effective thermal conductivities of these

65 materials, including the formulation of an interfacial layer, Brownian motion of the

66 nanoparticles, ballistic transport of energy carriers, and structural effects. Most of the

67 research has focused on thermal conductivity; however, the influence of nanoparticles

68 on the specific heat capacity is still unclear [24].

69   Das et al. [25,26] investigated the specific heat capacity of nanofluids using a

70 mixture of water and ethylene glycol as the base fluid. Silica, zinc oxide, and alumina

71 nanoparticles were used and results indicated that the c_p decreased with an increase in

72 the nanoparticle concentration, but increased with increasing temperature. Similar

73 results were found by Zhou et al. [27] with CuO nanofluids, Zhou and Ni [28] with

74 Al_2O_3 nanofluids, and Elias et al. [29] with Al_2O_3 nanofluids. It seems that for

75 conventional nanofluids (those with water, oil, ethylene glycol, or alcohol as the base

76 fluid), the specific heat capacity is reduced by doping with nanoparticles. However,

77 with molten salt or an ionic liquid as the base fluid, the influence of adding

78 nanoparticles had the opposite effect. He et al. [30] prepared a carbonate salt/carbon

79 nanomaterial composite to enhance the performance of a high-temperature salt. Both

80 the specific heat capacity and thermal conductivity were significantly enhanced. Ding

81 et al. [31] prepared a mixture of solar salt and nanoparticles by mechanic grinding and

82 mixing. An enhancement of 10.48% in the specific heat capacity was obtained by

83 adding CuO nanoparticles up to a mass concentration of 0.1%. Beyond this

84 concentration, however, the enhancement worsened, and the specific heat capacity

85 deteriorated at a concentration of 1.5%. Ho and Pan [32] formulated the Hitec-based

86 Al_2O_3 nanocomposite in a specially designed rid at high temperature. They studied the

87 effects of nanoparticle concentration on the specific heat capacities of nanocomposites

88 and found that the optimal concentration was 0.063% with an enhancement of 20%.

89 Jo and Banerjee [33,34] investigated the influence of graphite and multi-walled

90 carbon nanotubes (MCNT) on the specific heat capacity of a carbonate mixed salt. An

91 enhancement greater than 20% was obtained, and molecular dynamics simulations

92 (MDS) were carried out to better understand the tremendous improvement. Shin et al.

93 [35–39] performed a series investigation on carbonate salt-based SiO_2

94 nanocomposites. The enhancement in the specific heat capacity varied from 5% to

95 30%, and they proposed three models to explain the enhancement: (1) a higher c_p for

96 the silica nanoparticles than that of the bulk material; (2) solid-fluid interaction energy;

97 and (3) a semi-solid layer formulation of liquid molecules surrounding the

98 nanoparticles. Lu et al. [40] and Schuller et al. [41] prepared solar salt-based Al_2O_3

99 nanocomposites using a similar method, but obtained contrary results. The former

100   showed a decrease in the c_p, while in the latter it was enhanced 30.6%.

101   Though several studies have reported increased specific heat capacity, the rules

102 and mechanisms involved for this increase in molten salts with nanoparticle doping

103 are still insufficient. Most explanations about the significant enhancement of c_p were

104 based on some assumptions. In the present work, different mass fractions of solar

105 salt-based nanofluids were investigated using experimental measurements and

106 simulations. The nanomaterials were prepared by a dissolution method, and the specific

107 heat capacity was measured by a differential scanning calorimeter (DSC) using the

108 sapphire method. Material morphology analysis was conducted by a scanning electron

109 microscope. The effects of nanoparticles on the potential energy were then analyzed

110 by molecular dynamics simulations.

2. Experiment

2.1 Nanocomposite synthesis

113   In this study, we used the liquid solution method proposed by Shin et al. [36] to

114 formulate the nanocomposites. Sodium nitrate and potassium nitrate were procured

115 from Tianjin Fengchuan Chemical Reagent Technologies Co., Ltd., both with purities

116 above 99.0%. Al_2O_3 nanoparticles were purchased from Beijing Dk Nanotechnology

117 Co. Ltd. The average diameter was about 20 nm and the purity was 99.99%. The

118 procedure followed for obtaining the molten salt nanomaterial is illustrated in figure 1.

119 Initially, 5 mg of Al_2O_3 nanoparticles were added to 20 mL of deionized water, which

120 was then stirred for 20 min to form a suspension. Then, the suspension was sonicated

121 for 60 min in an ultrasonicator (PS-100A, Jieken Ultrasonic Cleaner Limited, China) at

122 a frequency of 40 kHz to ensure good dispersion and to minimize the potential

123 agglomeration of nanoparticles. After that, different weights of the solar salt were

124 dissolved in the suspension, so that the mass fraction of nanoparticles varied from 0.5%

125 to 2.0%. The mixture was ultrasonicated for another 60 min to guarantee uniformity of

126 the mixture. After sonication, the solution was then heated in a vacuum drying oven at

127 atmospheric pressure with a temperature setting of 110 °C, according to the research

128 of Jo [34] that evaporation temperature has little effect on the results. It was heated for

129 7 hours to obtain the dehydrated salt, which was the testing material for the DSC. All

130 powders were weighed using an electronic microbalance (Sartorius MC 21S). It should

131 be noted that there is no dispersing agent used in the preparation procedure.

2.2 Measurement of specific heat capacity

The specific heat capacities of the samples were measured based on the sapphire method using a DSC (204F1, NETZSCH). Aluminum pans were used to contain the samples, and the sample masses ranged from 5 mg to 15 mg. To protect the instrument from potential damage, the aluminum pans were covered with pierced lids. In the sapphire method, the heat flow through an empty pan, an aluminum pan with sapphire, and an aluminum pan with a prepared sample is measured. Then, using the three results and the specific heat capacity of sapphire, the specific heat capacity of each sample is calculated. The samples were heated to 50 °C and maintained at this temperature for 5 min to stabilize the calorimeter signal. A ramping rate of 20 °C/min was then applied, with the end temperature set to 450 °C. The sample was maintained at 450 °C for 5 min to ensure signal stability. Each sample was measured 3 times following the same procedure.

2.3 Uncertainty analysis

Uncertainties in the experimental results are dependent on the measurement deviations for each of the parameters, including mass and heat flow. The specific heat capacity was determined by Equation (1):

$$c_{p,s} = c_{p,sapp} \cdot \frac{\Delta q_s \cdot m_{sapp}}{\Delta q_{sapp} \cdot m_s} \tag{1}$$

where c_p is the specific heat capacity, q is the heat flow, m is the weight, and the subscripts s and sapp denote sample and sapphire. Taking f as a function of several independent parameters f_i, and each uncertainty as Δf_i, then the uncertainty of the experiment can be expressed as:

$$d(\ln f) = \sum_{i=1}^{n} \left| \frac{\partial \ln f}{\partial f_i} \right| \Delta f_i \tag{2}$$

The accuracy of the electronic balance was ± 0.005 mg, and the accuracy of the heat flow measurement was ± 0.1 μW. Hence, the maximum measurement uncertainty of the specific heat capacity was estimated to be 2.4%.

3. Molecular dynamics simulations

Molecular dynamics (MD) simulations were performed to explore interactions between the nanoparticles and solvent molecules using the Large-scale Atomic/Molecular Massively Parallel Simulator (LAMMPS) package. Initially, one Al_2O_3 nanoparticle fixed with a diameter of 2 nm was placed in the center of the simulation box and the solar salt molecules were placed randomly in the box, as shown in figure 2. The length of the simulation box was varied to adjust the nanoparticle mass concentration from 0% to 2.0%.

The Lennard-Jones (L-J) potential with long-range Coulombic force was employed to calculate the interaction between two non-bonded atoms, as shown in Equation (3), where E(r) is the potential of the two atoms, r is their distance from each other, q_i and q_j are the charges on atoms i and j, respectively, ε is the potential well depth, and σ is the finite distance at which the inter-particle potential is zero. The L-J parameters between different atomic species were calculated by the Berthlot mixing rule [42], as shown in Equation (4). In addition, bond stretching, bond bending, and torsion were considered for the bonded interactions, as shown in Equation (5), where r is bond length, θ is bond angle, ϕ is torsional angle, k_s, k_b, k_t are stretching, bending and torsional constants, respectively. All parameters used for the different atoms in the MD simulation are listed in Table 1.

$$E\left(r\right) = \frac{q_i q_j}{r} + 4\varepsilon\left[\left(\frac{\sigma}{r}\right)^{12} - \left(\frac{\sigma}{r}\right)^6\right] \tag{3}$$

$$\varepsilon_{i,j} = \sqrt{\varepsilon_i \cdot \varepsilon_j}, \quad \sigma_{i,j} = \frac{\left(\sigma_i + \sigma_j\right)}{2} \tag{4}$$

$$E = k_s \cdot \left(r - r_0\right)^2 + k_b \cdot \left(\theta - \theta_0\right) + k_t \cdot \left(1 + d \cdot \cos\left(n\phi\right)\right) \tag{5}$$

Since the solar salt molecules were randomly placed in the simulation box, it is highly possible that there would be overlapping atoms, which would result in non-physical interactions. Hence, an energy minimization step was implemented to redistribute the atoms. During this step, the temperature of the system was reduced to zero K. Afterwards, a microcanonical ensemble was used to perform the relaxation procedure. Subsequently, the system temperature was raised to 650 K. A canonical Nose-Hoover thermostat (NVT integration, with a constant number of atoms N, volume of the system V, and temperature T controlled through direct temperature scaling) was used for the temperature range from 650 to 800 K to obtain the specific

190   heat capacity of the system.

4. Results and Discussion

4.1 Specific heat capacity results

193   The solar salt was doped with Al_2O_3 nanoparticles with an average diameter of 20
194   nm at mass fractions of 0.5%, 1.0%, 1.5%, and 2.0%. To guarantee the accuracy of the
195   instrument, the melting temperature and enthalpy of Sn and Bi were measured and
196   good agreement was shown with reference values, as shown in table 2.
197   Figure 3 shows the variations in the specific heat capacities of the base salt and
198   nanocomposite mixtures in the full temperature range (80 °C to 400 °C). There are two
199   peaks in the temperature range, at about 130 °C and 227 °C, which indicate the phase
200   change temperatures. The peak at about 130 °C was formed by the solid-solid phase
201   change of the eutectic salt and the peak at about 227 °C was formed by the solid-liquid
202   phase change, agreeing with data from the literature [43] in which the respective peaks
203   were at 130.4 °C and 224.8 °C. The specific heat capacity of the base salt in the liquid
204   phase had an average value of 1.56 J/(g·K), showing a good agreement with values in
205   the literature of 1.50 to 1.53 J/(g·K) [44], a less than 5% error. It also can be seen that
206   the specific heat capacities of the samples changed only slightly with temperature,
207   indicating that temperature does not substantially affect the specific heat capacities of
208   these samples. In other words, the specific heat capacity is nearly independent of
209   temperature. Meanwhile, we can see that with an increase in the mass fraction of the
210   Al_2O_3 nanoparticles, the specific heat capacity of the samples increased.
211   Thermal energy storage (TES) capacity is an important parameter for TES systems,
212   since it influences the scope of the system and the operating cost. The TES capacity (Q)
213   was calculated as below.

$$ Q = \frac{\int_{260°C}^{400°C} h(T)dT}{mdT / dt} \tag{6} $$

215   where h is the heat flow, T is the working temperature, m is the weight of the sample,
216   and dT/dt is the heating rate. The total Q for pure base salt and after adding 0.5, 1.0, 1.5,
217   and 2.0 wt.% nanoparticles were 219.03, 223.01, 231.07, 233.84, and 236.32 kJ/kg in
218   the working temperature range of 260–400 °C, respectively. This indicates that the Q
219   value of the nanocomposite with ~2.0 wt.% nanoparticles has a maximum increase of
220   17.29 kJ/kg. Figure 4 plots Q versus temperature for pure base salt and after adding

different amounts of nanoparticles. With increasing the nanoparticle mass fraction, the TES capacity increases in the working temperature range of 260–400 °C.

Usually, the specific heat capacity of the mixture is calculated using a simple mixing model. The mixing model is based on the assumption of thermal equilibrium between the particles and fluid and can be expressed as:

$$c_{p,nf} = \frac{m_{np}c_{p,np} + m_s c_{p,s}}{m_{nf}} \tag{7}$$

where c_p is the specific heat capacity, m is the mass, and the subscripts nf, np, and s denote the property values of the nanofluid, nanoparticle, and salt, respectively. The specific heat capacity of the base salt and Al_2O_3 particles are 1.56 J/(g·K) and 1.12 J/(g·K), respectively, as measured in present work. Figure 5 shows a comparison between the experimental value and the value predicted by the simple mixing model. The measured average specific heat capacity of the base salt and nanocomposites, from lowest to highest concentration, were 1.56 J/(g·K), 1.59 J/(g·K), 1.65 J/(g·K), 1.67 J/(g·K), and 1.69 J/(g·K), respectively. This indicates that the specific heat capacity of the nanocomposite with an Al_2O_3 particle concentration of about 2.0% by weight has a maximum enhancement of about 8.3%. However, the prediction values decreased with an increase in the nanoparticle mass fraction, indicating that the simple mixing model is not applicable in the evaluation of the specific heat capacity of a nanocomposite.

4.2 Material Characterization

Since the specific heat capacity has a close relationship with the phase or structure of the material, scanning electron microscope (SEM) (Quanta 200FEG) was used to perform material characterization analyses. Figure 6 shows an SEM image of the salt with various concentrations of nanoparticles after the DSC measurement. The surface of the base salt was relatively smooth and had few visible structures. With the addition of nanoparticles, some punctate and nubby microstructures appear (Figure 6 a). Adding more nanoparticles (Figure 6 b, c, and d) increases the quantity of these microstructures and decreases the structure size. This kind of microstructure results in an increase of the surface area. Due to the mismatch of vibrational density of states between liquid and solid phase, there will be an interfacial thermal resistance, well known as Kapitza resistance [45]. With the increase of the surface area, the total interfacial thermal resistance will increase significantly [46,47], which will provide additional thermal storage being responsible for enhancing the specific heat capacity.

4.3 Molecular dynamics simulations

To verify the accuracy of the MD simulations, the densities and c_p values of the solar salt mixed with different mass concentrations of nanoparticles were calculated. Figure 7 shows the comparison of density results from the MD simulation system and theoretical calculation using Equation (8). Good agreement was obtained.

$$\rho_{nf} = \varphi\rho_p + (1-\varphi)\rho_f \tag{8}$$

where φ is the volume fraction of nanoparticles and the subscripts p and f denote the nanoparticles and fluid, respectively.

In figure 8, it can be seen that the total energy of the ensemble changes linearly with temperature for various nanoparticle mass concentrations, with an Adj. $R^2 >$ 0.998. Hence, the c_p of the solar salt-based nanofluid is almost constant in the temperature range of 650-800 K.

The specific heat capacity, c_p, is calculated as:

$$c_p = \frac{\Delta E}{\Delta T \cdot V \cdot \rho} \tag{9}$$

where ΔE is the energy change, ΔT is the temperature change, V is the volume, and ρ is the density of the ensemble. Figure 9 shows the experimental and simulated c_p values with different nanoparticle mass concentrations. Acceptable agreement was obtained—for pure base salt, c_p obtained from the MD simulation was 1.491 J/(g·K) with an error of about -4.42% compared with the experimental value of 1.56 J/(g·K). The same trend with nanoparticle concentration was also obtained: c_p increased with increasing nanoparticle mass concentration, and at 2.0 wt.% nanoparticles, the c_p enhancements were 6.24% and 8.33%, respectively, for the simulation and experiment.

In order to explain this unusual enhancement of the c_p, we analyzed the energy components and interaction for each atomic type (figure 10) in the simulation. The energy of each atom can be divided into two parts: the kinetic energy (E_{ke}) and the potential energy (E_{pe}), as shown in Equation (10).

$$E = E_{ke} + E_{pe} \tag{10}$$

where the potential energy is composed of Van der Waals energy (E_{vdw}), Coulombic energy (E_{coul}), long-range k-space energy (E_{long}), and molecular energy (E_{mol}). From Figure 10, we can see that there was no significant change for E_{ke}, E_{vdw}, and E_{long}, while E_{pe} increased with the nanoparticle mass concentration due to the increase of

286 E_{coul} and E_{mol}. In other words, adding nanoparticles does not change the movement of
287 molecules, the interaction potential between two atoms and the energy in k space.
288 Figure 10 (b) shows the energy of three different intermolecular interactions in NO_3^-.
289 All of them change only slightly, indicating that the influence of added nanoparticles
290 on the molecular structure of NO_3^- is negligible. Hence, the slight increase in E_{mol} per
291 atom is due to the high molecular energy of Al_2O_3. Only the Coulombic energy
292 change significantly for different nanoparticle mass fractions. Hence, the
293 enhancement of c_p is mainly due to the increase of the Coulombic energy, which can
294 also explain the different effects on c_p from adding nanoparticles to conventional base
295 fluids and molten salts. Since there are more ions in molten salt, the influence of the
296 Coulombic force is more significant.

Conclusion

298 In this study, the specific heat capacities of a binary nitrate salt and
299 nanocomposites with different mass fractions of added nanoparticles (0, 0.5, 1.0, 1.5,
300 and 2.0 wt.%, respectively) were investigated. The nanocomposites were synthesized
301 using a solution method. DSC was employed to measure the specific heat capacity.
302 Results show that the enhancement of the specific heat capacity of nanocomposites
303 ranges from 1.9% to 8.3% with an increase in the mass fraction of added
304 nanoparticles. The simple mixing model failed to predict the specific heat capacity of
305 the molten salt-based nanofluids. Material characterization analyses were carried out
306 using SEM. From the SEM images, we can see the formulation of punctate or nubby
307 nanostructures, which may induce the enhancement of specific heat capacity through
308 the enlarged specific surface area. The influence of nanoparticles on the energy
309 components of each atomic type was analyzed by molecular dynamics simulations.
310 Results indicate that the change in Coulombic energy per atom contributes the
311 greatest portion of the enhanced c_p.

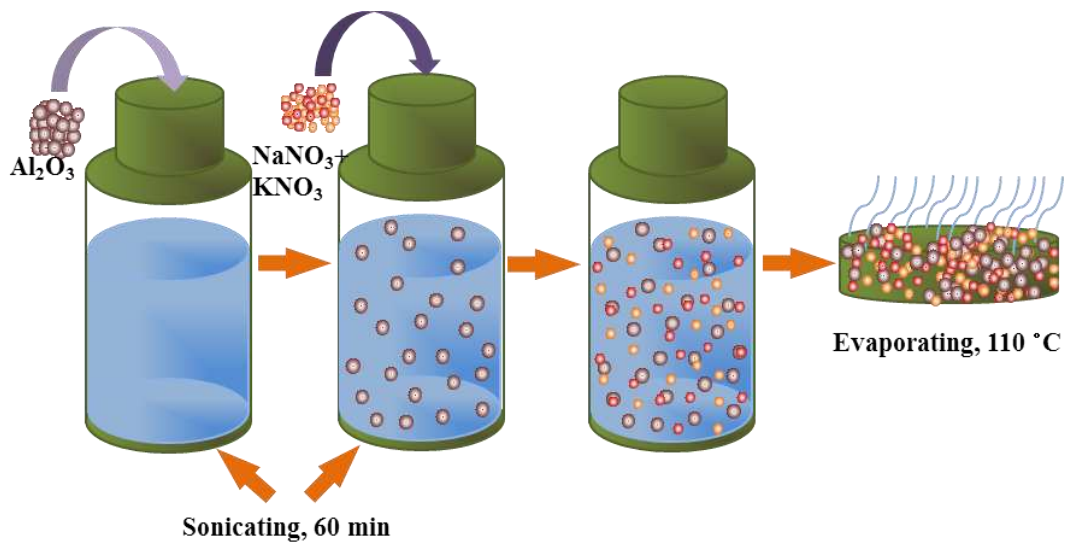## Acknowledgements

318   BRETIV. 201315).

References

320   [1]   Owusu PA, Asumadu-Sarkodie S. A review of renewable energy sources, sustainability issues
321   and climate change mitigation. Cogent Eng 2016;3:1–14. doi:10.1080/23311916.2016.1167990.

322   [2]   Kim MH, Kim H, Lee KS, Kim DR. Frosting characteristics on hydrophobic and
323   superhydrophobic surfaces: A review. Energy Convers Manag 2017;138:1–11.
324   doi:10.1016/j.enconman.2017.01.067.

325   [3]   Mahian O, Kianifar A, Kalogirou SA, Pop I, Wongwises S. A review of the applications of
326   nanofluids in solar energy. Int J Heat Mass Transf 2013;57:582–94.
327   doi:10.1016/j.ijheatmasstransfer.2012.10.037.

328   [4]   Kim MH, Kim H, Kim DR, Lee KS. A novel louvered fin design to enhance thermal and
329   drainage performances during periodic frosting/defrosting conditions. Energy Convers Manag
330   2016;110:494–500. doi:10.1016/j.enconman.2015.11.028.

331   [5]   Kundu B, Lee KS. Effects of psychrometric properties on fin performances of minimum
332   envelope shape of wet fins. Energy Convers Manag 2016;110:481–93.
333   doi:10.1016/j.enconman.2015.09.054.

334   [6]   Park SJ, Jang D, Yook SJ, Lee KS. Optimization of a chimney design for cooling efficiency of a
335   radial heat sink in a LED downlight. Energy Convers Manag 2016;114:180–7.
336   doi:10.1016/j.enconman.2016.02.024.

337   [7]   Jang D, Park SJ, Lee KS. Thermal performance of a PCB channel heat sink for LED light bulbs.
338   Int J Heat Mass Transf 2015;89:1290–6. doi:10.1016/j.ijheatmasstransfer.2015.06.027.

339   [8]   Mahian O, Kianifar A, Sahin AZ, Wongwises S. Performance analysis of a minichannel-based
340   solar collector using different nanofluids. Energy Convers Manag 2014;88:129–38.
341   doi:10.1016/j.enconman.2014.08.021.

342   [9]   Meibodi SS, Kianifar A, Mahian O, Wongwises S. Second law analysis of a nanofluid-based
343   solar collector using experimental data. J Therm Anal Calorim 2016;126:617–25.
344   doi:10.1007/s10973-016-5522-7.

345 [10] Crabtree GW, Lewis NS. Solar energy conversion. Phys Today 2007;60:37–42.
346   doi:10.1063/1.2718755.

347 [11] Price H, Lüpfert E, Kearney D, Zarza E, Cohen G, Gee R, et al. Advances in parabolic trough
348   solar power technology. J Sol Energy Eng 2002;124:109. doi:10.1115/1.1467922.

349 [12] Salavati S, Kianifar A, Niazmand H, Mahian O, Wongwises S. Experimental investigation on the
350   thermal efficiency and performance characteristics of a flat plate solar collector using SiO_2/EG–
351   water nanofluids. Int Commun Heat Mass Transf 2015;c:71–5.
352   doi:10.1016/j.icheatmasstransfer.2015.02.011.

353 [13] Mahian O, Kianifar A, Sahin AZ, Wongwises S. Entropy generation during Al_2O_3/water
354   nanofluid flow in a solar collector: Effects of tube roughness, nanoparticle size, and different
355   thermophysical models. Int J Heat Mass Transf 2014;78:64–75.
356   doi:10.1016/j.ijheatmasstransfer.2014.06.051.

357 [14] Lu J, Yu T, Ding J, Yuan Y. Thermal storage performance of molten salt thermocline system
358   with packed phase change bed. Energy Convers Manag 2015;102:267–74.
359   doi:10.1016/j.enconman.2014.10.049.

360 [15] Peng Q, Yang X, Ding J, Wei X, Yang J. Design of new molten salt thermal energy storage
361   material for solar thermal power plant. Appl Energy 2013;112:682–9.
362   doi:10.1016/j.apenergy.2012.10.048.

363 [16] Zhang HL, Baeyens J, Degrève J, Cacères G. Concentrated solar power plants: Review and
364   design methodology. Renew Sustain Energy Rev 2013;22:466–81.
365   doi:10.1016/j.rser.2013.01.032.

366 [17] Boerema N, Morrison G, Taylor R, Rosengarten G. Liquid sodium versus Hitec as a heat transfer
367   fluid in solar thermal central receiver systems. Sol Energy 2012;86:2293–305.
368   doi:10.1016/j.solener.2012.05.001.

369 [18] Dunn RI, Hearps PJ, Wright MN. Molten-salt power towers: Newly commercial concentrating
370   solar storage. Proc. IEEE, vol. 100, 2012, p. 504–15. doi:10.1109/JPROC.2011.2163739.

371 [19] Jo B, Banerjee D. Effect of solvent on specific heat capacity enhancement of binary molten
372   salt-based carbon nanotube nanomaterials for thermal energy storage. Int J Therm Sci
373   2015;98:219–27. doi:10.1016/j.ijthermalsci.2015.07.020.

374 [20] Ye F, Ge Z, Ding Y, Yang J. Multi-walled carbon nanotubes added to Na_2CO_3/MgO composites
375   for thermal energy storage. Particuology 2014;15:56–60. doi:10.1016/j.partic.2013.05.001.

376 [21] Choi SUS, Eastman JA. Enhancing thermal conductivity of fluids with nanoparticles. ASME Int.
377   Mech. Eng. Congr. Expo., vol. 66, 1995, p. 99–105. doi:10.1115/1.1532008.

378 [22] Sadeghinezhad E, Mehrali M, Saidur R, Mehrali M, Tahan Latibari S, Akhiani AR, et al. A
379   comprehensive review on graphene nanofluids: Recent research, development and applications.
380   Energy Convers Manag 2016;111:466–87. doi:10.1016/j.enconman.2016.01.004.

381 [23] Wen D, Lin G, Vafaei S, Zhang K. Review of nanofluids for heat transfer applications.
382   Particuology 2009;7:141–50. doi:10.1016/j.partic.2009.01.007.

383 [24] Sekhar YR, Sharma K V. Study of viscosity and specific heat capacity characteristics of
384   water-based Al_2O_3 nanofluids at low particle concentrations. J Exp Nanosci 2017;10:86–102.
385   doi:10.1080/17458080.2013.796595.

386 [25] Namburu PK, Kulkarni DP, Dandekar A, Das DK. Experimental investigation of viscosity and
387   specific heat of silicon dioxide nanofluids. Micro Nano Lett 2007;2:67 –71. doi:10.1049/mnl.

388 [26] Vajjha RS, Das DK. Specific heat measurement of three nanofluids and development of new
389   correlations. J Heat Transfer 2009;131:71601. doi:10.1115/1.3090813.

390 [27] Wang BX, Zhou LP, Peng XF, Du XZ, Yang YP. On the specific heat capacity of CuO nanofluid.
391   Adv Mech Eng 2010;2010. doi:10.1155/2010/172085.

392 [28] Zhou SQ, Ni R. Measurement of the specific heat capacity of water-based Al_2O_3 nanofluid. Appl
393   Phys Lett 2008;92:93123. doi:10.1063/1.2890431.

394 [29] Elias MM, Mahbubul IM, Saidur R, Sohel MR, Shahrul IM, Khaleduzzaman SS, et al.
395   Experimental investigation on the thermo-physical properties of Al_2O_3 nanoparticles suspended
396   in car radiator coolant. Int Commun Heat Mass Transf 2014;54:48–53.
397   doi:10.1016/j.icheatmasstransfer.2014.03.005.

398 [30] Tao YB, Lin CH, He YL. Preparation and thermal properties characterization of carbonate
399   salt/carbon nanomaterial composite phase change material. Energy Convers Manag
400   2015;97:103–10. doi:10.1016/j.enconman.2015.03.051.

401 [31] Lasfargues M, Geng Q, Cao H, Ding Y. Mechanical dispersion of nanoparticles and its effect on
402   the specific heat capacity of impure binary nitrate salt mixtures. Nanomaterials 2015;5:1136–46.
403   doi:10.3390/nano5031136.

404 [32] Ho MX, Pan C. Optimal concentration of alumina nanoparticles in molten Hitec salt to maximize
405 its specific heat capacity. Int J Heat Mass Transf 2014;70:174–84.
406 doi:10.1016/j.ijheatmasstransfer.2013.10.078.

407 [33] Jo B, Banerjee D. Enhanced specific heat capacity of molten salt-based nanomaterials: Effects of
408 nanoparticle dispersion and solvent material. Acta Mater 2014;75:80–91.
409 doi:10.1016/j.actamat.2014.05.005.

410 [34] Jo B, Banerjee D. Effect of dispersion homogeneity on specific heat capacity enhancement of
411 molten salt nanomaterials using carbon nanotubes. J Sol Energy Eng 2014;137:11011.
412 doi:10.1115/1.4028144.

413 [35] Shin D, Banerjee D. Enhanced thermal properties of SiO_2 nanocomposite for solar thermal
414 energy storage applications. Int J Heat Mass Transf 2015;84:898–902.
415 doi:10.1016/j.ijheatmasstransfer.2015.01.100.

416 [36] Shin D, Banerjee D. Enhanced specific heat of silica nanofluid. J Heat Transfer 2011;133:24501.
417 doi:10.1115/1.4002600.

418 [37] Shin D, Banerjee D. Enhanced specific heat capacity of nanomaterials synthesized by dispersing
419 silica nanoparticles in eutectic mixtures. J Heat Transfer 2013;135:32801.
420 doi:10.1115/1.4005163.

421 [38] Tiznobaik H, Shin D. Experimental validation of enhanced heat capacity of ionic liquid-based
422 nanomaterial. Appl Phys Lett 2013;102:173906. doi:doi:http://dx.doi.org/10.1063/1.4801645.

423 [39] Tiznobaik H, Shin D. Enhanced specific heat capacity of high-temperature molten salt-based
424 nanofluids. Int J Heat Mass Transf 2013;57:542–8.
425 doi:10.1016/j.ijheatmasstransfer.2012.10.062.

426 [40] Lu MC, Huang CH. Specific heat capacity of molten salt-based alumina nanofluid. Nanoscale
427 Res Lett 2013.

428 [41] Schuller M, Shao Q, Lalk T. Experimental investigation of the specific heat of a nitrate–alumina
429 nanofluid for solar thermal energy storage systems. Int J Therm Sci 2015;91:142–5.
430 doi:10.1016/j.ijthermalsci.2015.01.012.

431 [42] Li L, Zhang Y, Ma H, Yang M. An investigation of molecular layering at the liquid-solid
432 interface in nanofluids by molecular dynamics simulation. Phys Lett A 2008;372:4541–4.
433 doi:10.1016/j.physleta.2008.04.046.

434 [43] Xiao J, Huang J, Zhu P, Wang C, Li X. Preparation, characterization and thermal properties of
435 binary nitrate salts/expanded graphite as composite phase change material. Thermochim Acta
436 2014;587:52–8. doi:10.1016/j.tca.2014.04.021.

437 [44] Betts MR. The effects of nanoparticle augmentation of nitrate thermal storage materials for use
438 in concentrating solar power applications. A Thesis Maeter Sci 2011.

439 [45] Pollack GL. Kapitza Resistance. Rev Mod Phys 1969;41:48–81.
440 doi:10.1103/RevModPhys.41.48.

441 [46] Zain-ul-abdein M, Raza K, Khalid FA, Mabrouki T. Numerical investigation of the effect of
442 interfacial thermal resistance upon the thermal conductivity of copper/diamond composites.
443 Mater Des 2015;86:248–58. doi:10.1016/j.matdes.2015.07.059.

444 [47] Hu H, Sun Y. Effect of nanopatterns on Kapitza resistance at a water-gold interface during
445 boiling: A molecular dynamics study. J Appl Phys 2012;112:53508. doi:10.1063/1.4749393.

446
447

467
468
469
470
471
472
473
474
475
476
477
478
479
480
481
482

483

484

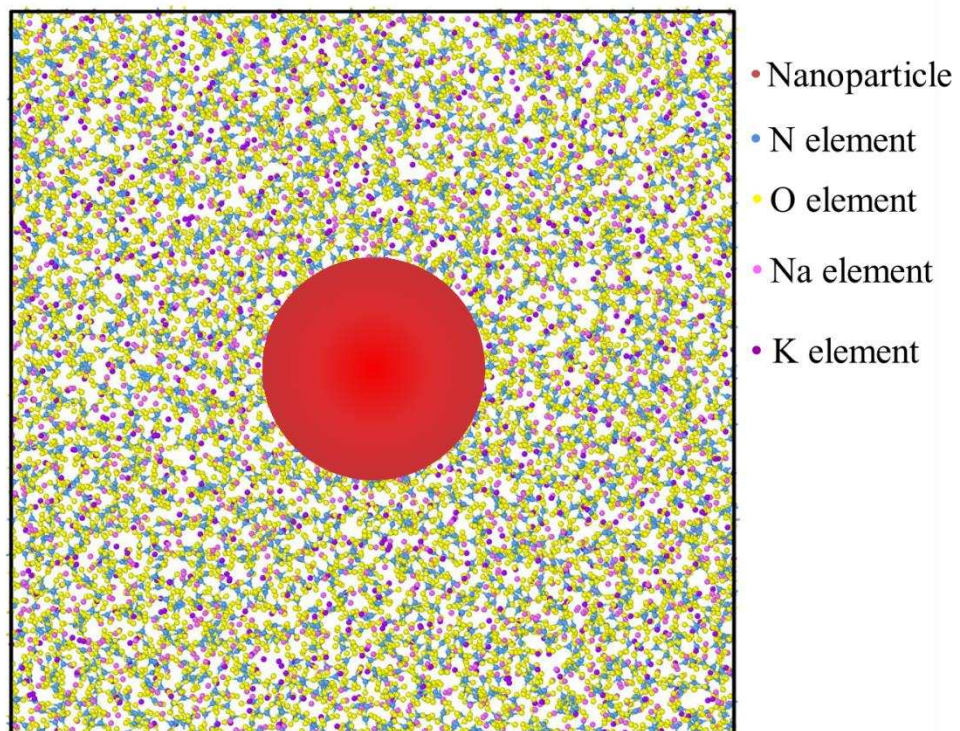Fig. 1 Nanocomposite preparation procedure

486
487
488
489

490
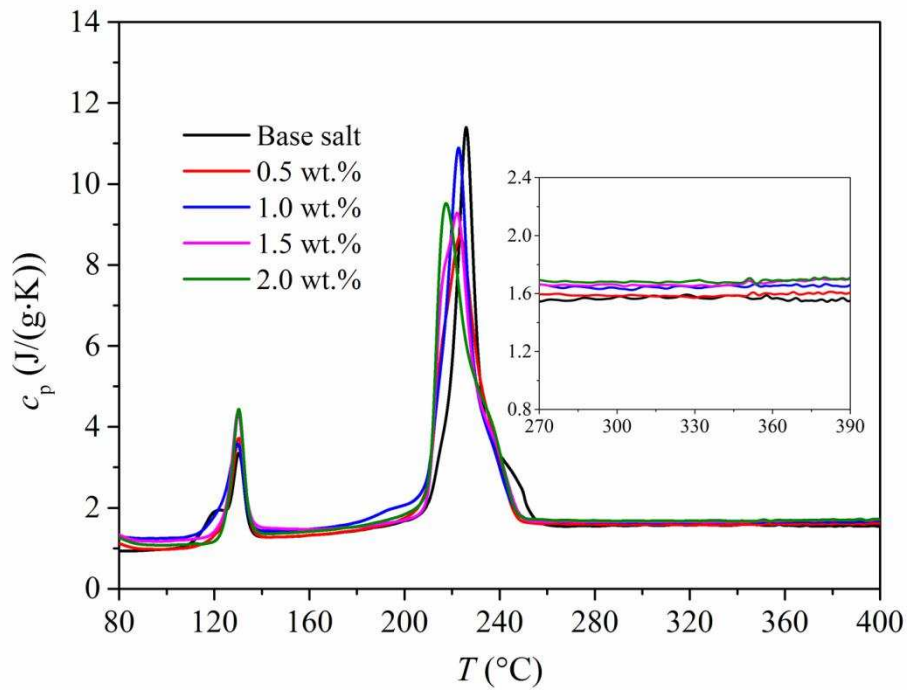
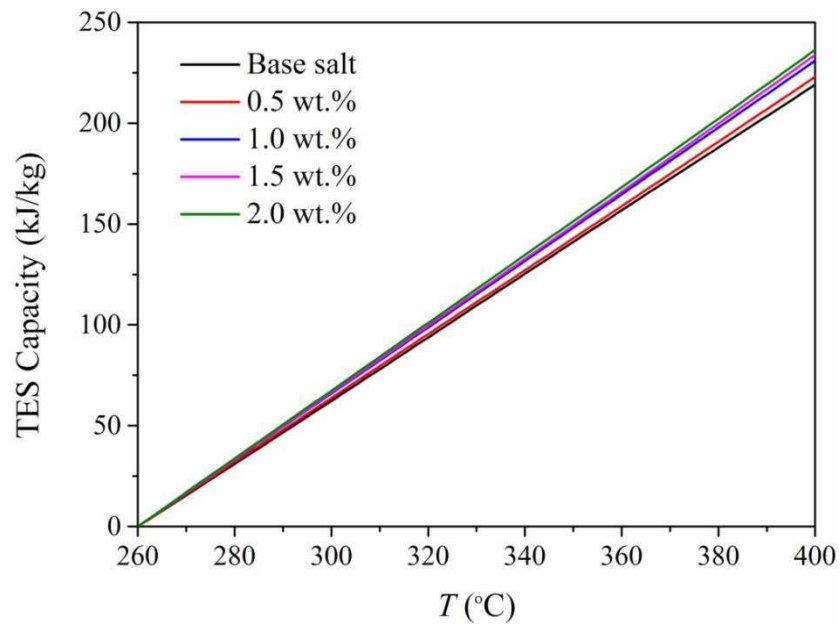Fig. 2 Simulation domain showing an Al_2O_3 nanoparticle surrounded by solar salt molecules

492
493

494

495

496

Fig. 3 Variation in c_p with temperature for the pure base salt and at different nanoparticle mass
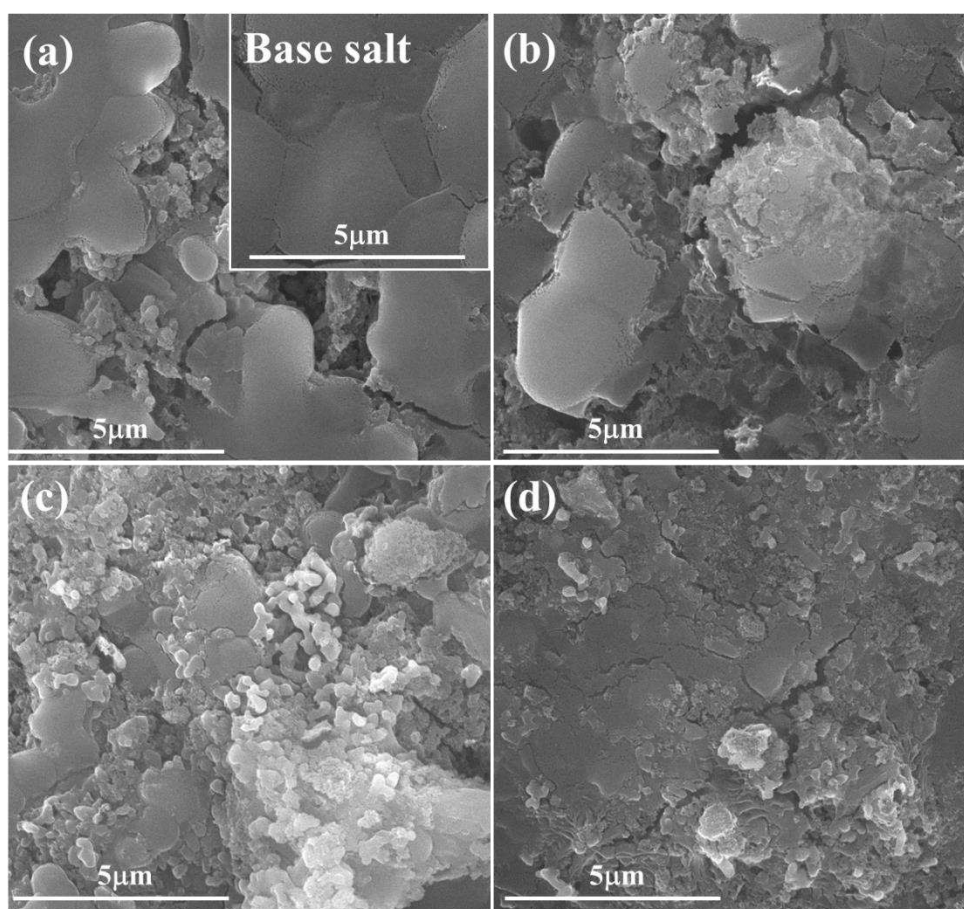
concentrations (0.5%, 1.0%, 1.5%, and 2.0%)

499

500

501

Fig. 4 Variation of TES capacity with temperature, for pure base salt and after adding different
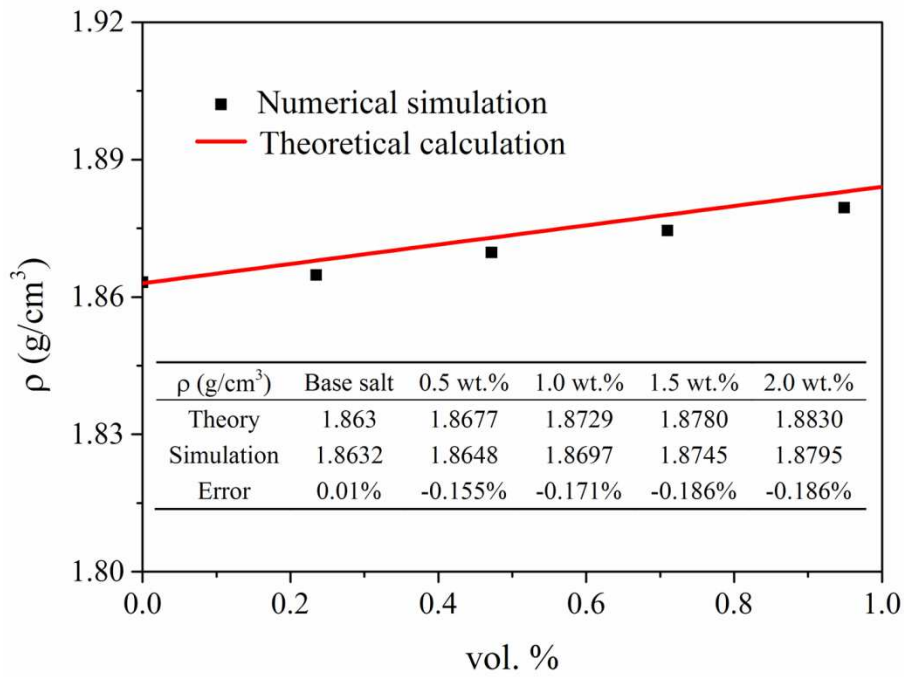
amounts of nanoparticles.

504

505
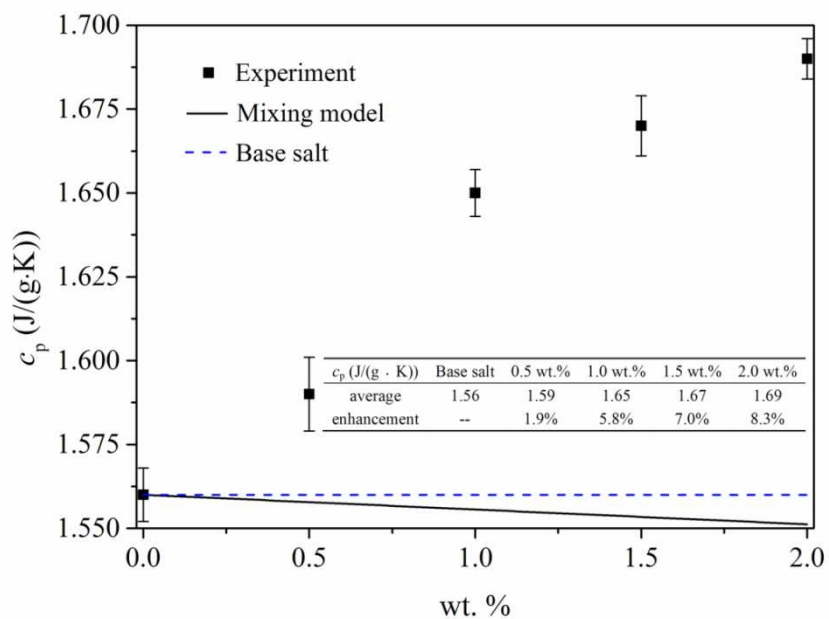
Fig. 5 Comparison of average experimental c_p values and the values predicted by the simple

mixing model

Fig. 6 SEM images of the salt with various nanoparticle concentrations after DSC measurement:

(a) 0.5 wt.%, (b) 1.0 wt.%, (c) 1.5 wt.%, and (d) 2.0 wt.%.
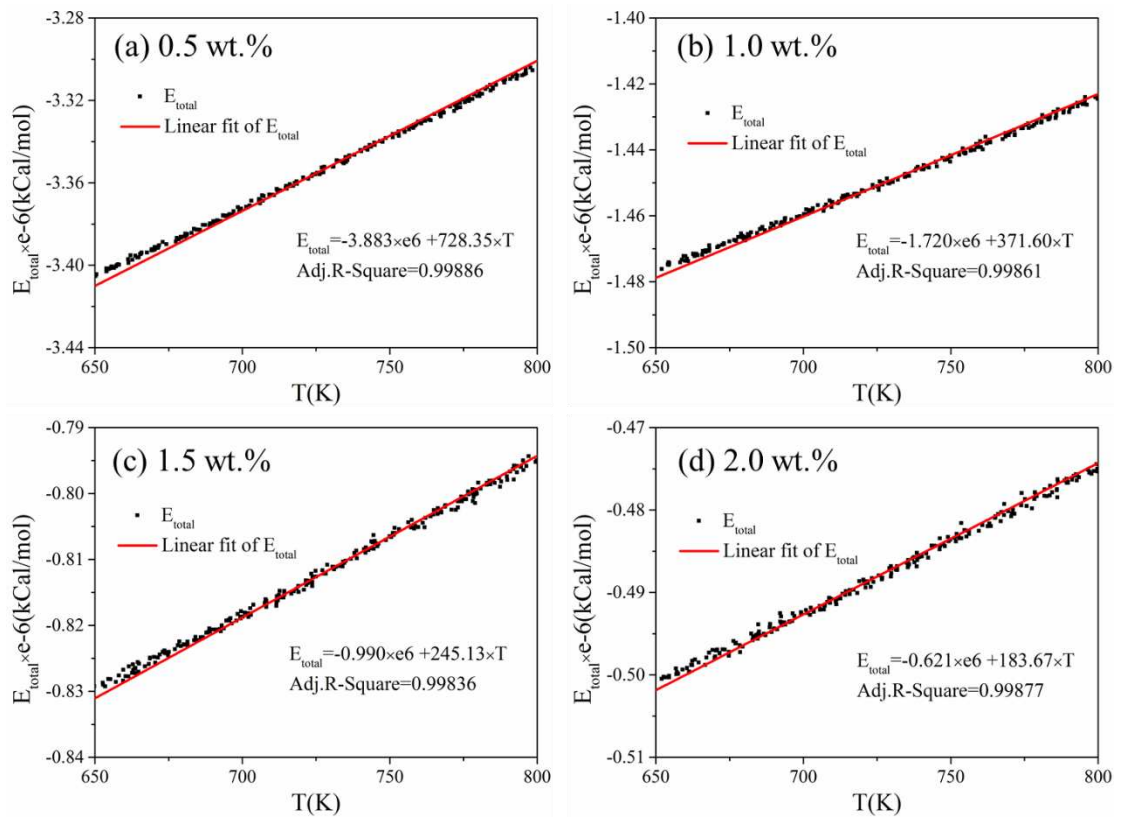
513

514

515   Fig. 7 Comparison between simulations and theoretical calculations of the densities of a solar salt

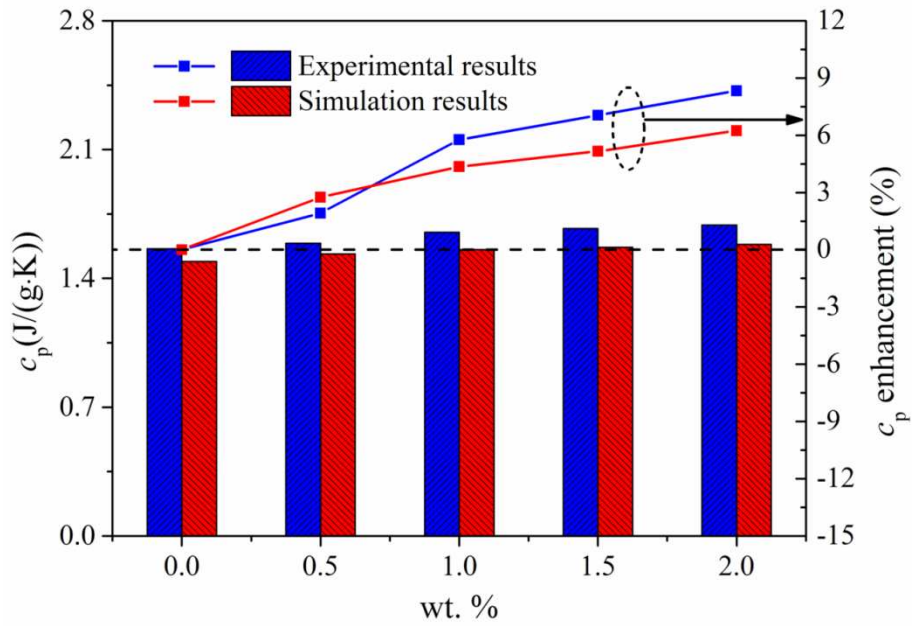516   mixed with nanoparticles

517

518

519   Fig. 8 Total energy of the ensemble versus temperature: (a) 0.5 wt.%, (b) 1.0 wt.% ₃, (c) 1.5 wt.%,

520   and (d) 2.0 wt.%

521

522
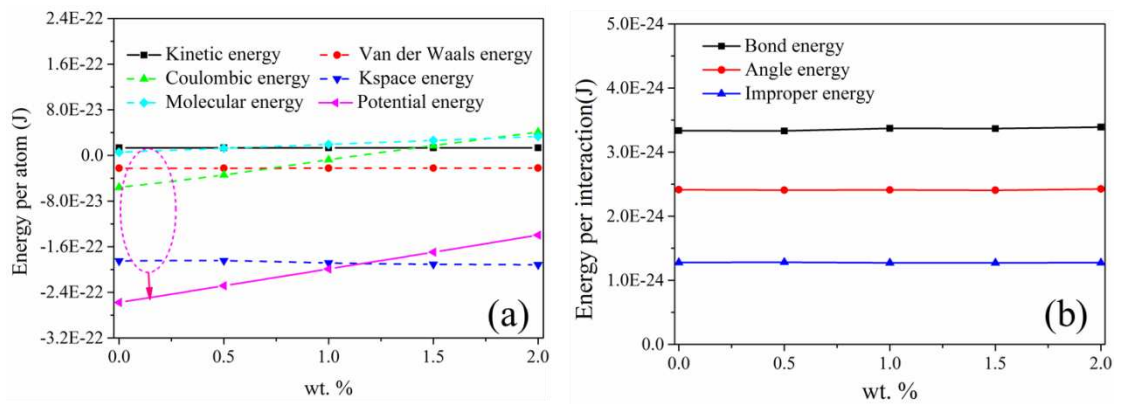

523

524   Fig. 9 Experimental and simulated c_p values with different nanoparticle mass concentrations in the

525   salts

526

527

528   Fig. 10 Potential and interaction energy analysis in the nanofluid system at 650 K

529

530

531

532

533

534

535

536

537

538

539

Table 1 Simulation parameters for the MD simulation

Lennard-Jones constants				
Material	Interaction	ε[kcal/mol]	σ[Å]	Charge
Al$_2$O$_3$	Al-Al	0.040	4.053	+1.5
	O-O	0.228	2.860	-1.0
	N-N	0.167	3.501	+0.95
Eutectic	O-O	0.228	2.860	-0.65
	Na-Na	1.607	1.897	+1.0
	K-K	5.451	3.197	+1.0

Bonded interaction							
Material	Stretching		Bending		Improper torsional		
	k_s	r_0	k_b	θ_0	k_t	d_t	ϕ_t
Al$_2$O$_3$	392.8	1.775	100.3 / 31.1	109.5 / 149.8	26.270	-1	2
Eutectic	525.0	1.268	105.0	120.0	26.270	-1	2

Table 2 Experimental validation

Sample	Melting temperature (°C)			Enthalpy (J/g)		
	Experiment	Reference	Error	Experiment	Reference	Error
Sn	232.2	231.9	0.13%	59.28	60.5	-2.02%
Bi	271.7	271.4	0.11%	52.12	53.1	-1.85%

561

562

Nomenclature	
Symbol	Meaning
c_p	specific heat capacity, J/(g·K)
q	heat flow, W
m	weight, kg
E	potential energy, J
r	distance between two atoms, Å
q	charge of atom, C
k	constant
d	sign convention constant
T	temperature, K
V	volume, m^3
Q	thermal energy storage capacity, J/g
h	heat flow, mW/mg
Greek symbols	
ε	potential well depth, kcal/mol
σ	finite distance for zero inter-particle potential, Å
θ	angle value, degrees
φ	volume fraction, -
ϕ	torsional angle, degrees
ρ	density, g/cm^3
Subscripts	
s	sample
sapp	sapphire
b	bending
t	torsional

563

564

565